

Thermodynamic stability and vibrational properties of multi-alkali antimonides

Julia Santana-Andreo^{1,2}, Holger-Dietrich Saßnick¹, and Caterina Cocchi^{1,2,3}

¹ Carl von Ossietzky Universität Oldenburg, Institute of Physics, 26129 Oldenburg, Germany

² Humboldt-Universität zu Berlin, Physics Department and IRIS Adlershof, 12489 Berlin, Germany

³ Carl von Ossietzky Universität Oldenburg, Center for Nanoscale Dynamics (CeNaD), 26129 Oldenburg, Germany

E-mail: julia.santana.andreo@uni-oldenburg.de,
caterina.cocchi@uni-oldenburg.de

Abstract. Modern advances in generating ultrabright electron beams have unlocked unprecedented experimental advances based on synchrotron radiation. Current challenges lie in improving the quality of electron sources with novel photocathode materials such as alkali-based semiconductors. To unleash their potential, a detailed characterization and prediction of their fundamental properties is essential. In this work, we employ density functional theory combined with machine learning techniques to probe the thermodynamic stability of various alkali antimonide crystals, emphasizing the role of the approximations taken for the exchange-correlation potential. Our results reveal that the SCAN functional offers an optimal trade-off between accuracy and computational costs to describe the vibrational properties of these materials. Furthermore, it is found that systems with a higher concentration of Cs atoms exhibit enhanced anharmonicities, which are accurately predicted and characterized with the employed methodology.

1. Introduction

Multi-alkali antimonides are semiconductors used as electron sources in particle accelerators [1–3]. Despite the persisting challenges in producing high-quality samples [4–6], the research on these materials is relentless. In terms of preparation, various recipes have been proposed based on co-evaporation [7–9] or sequential growth [10, 11]. The analysis of the produced photocathodes has focused both on their *operando* performance in accelerators [12–16] as well as on their physical properties [17–19]. These experimental efforts have been recently complemented by several theoretical studies aiming at an in-depth understanding of the fundamental characteristics of the materials [20–28] and their photoemission performance [29–33].

Computational research on photocathodes has been boosted by the advent of high-throughput screening methods which have enabled the exploration of large configurational spaces and the identification of optimal compounds for this specific application [26, 34, 35]. So far, corresponding efforts have been focused mainly on determining relative stability and energy levels without the inclusion of thermodynamic effects. This choice, however, considerably limits the predictive power of such calculations. Notable exceptions are given by some recent first-principle works on the thermoelectric and vibrational properties of multi-alkali antimonides [36, 37] even beyond the harmonic approximation [38, 39]. Yet, the validity of the chosen approximations on a variety of structures and compositions needs to be carefully checked.

In this work, we present a first-principle study on the thermodynamic and vibrational properties of binary and ternary alkali antimonide crystals. After assessing the performance of three popular exchange-correlation functionals of density-functional theory in terms of accuracy and computational costs, we analyze the phonon band structures within the harmonic approximation and beyond in a machine-learning-based computational framework. We find that all considered materials are dynamically stable at room temperature except for Cs₂KSb and that compounds with a larger concentration of Cs atoms exhibit enhanced anharmonic effects. Our results contribute to the characterization and understanding of multi-alkali antimonides and offer valuable information to predict their photoemission yield.

2. Computational methods

The results presented in this work are obtained by solving the Kohn-Sham (KS) equations [40] of density functional theory (DFT) [41]:

$$\left[-\frac{1}{2}\nabla^2 + v_s(\mathbf{r})\right]\psi_i(\mathbf{r}) = \varepsilon_i^{\text{KS}}\psi_i(\mathbf{r}). \quad (1)$$

In Eq. 1, formulated in atomic units, $\varepsilon_i^{\text{KS}}$ are the energy eigenvalues, $\psi_i(\mathbf{r})$ the wave functions, and $v_s(\mathbf{r})$ the effective KS potential including the contributions from the external, the Hartree, and the exchange-correlation (xc) potentials:

$$v_s(\mathbf{r}) = v_{\text{ext}}(\mathbf{r}) + v_H(\mathbf{r}) + v_{xc}(\mathbf{r}). \quad (2)$$

In contrast to v_{ext} and $v_H(\mathbf{r})$, the exact form of v_{xc} is unknown. Herein, we apply for this term the generalized gradient approximation (GGA) in the Perdew-Burke-Ernzerhof (PBE) parameterization [42], the SCAN functional [43] based on the meta-GGA, which has proven good performance in various material classes [44–46], and the range-separated hybrid functional HSE06 [47, 48].

All DFT calculations are performed with the VASP software suite [49–52] implementing the projector-augmented wave method. The investigated structures are fully optimized in terms of lattice vectors and atomic positions with a force threshold of 10^{-7} eV \AA^{-1} . In the self-consistent field calculations, an energy threshold of 10^{-9} eV and an energy cutoff of 500 eV are adopted. In line with earlier works [25, 38], the k-grids chosen to sample the Brillouin zones of all considered systems include $12 \times 12 \times 12$ points except for hexagonal NaK_2Sb where a $8 \times 8 \times 4$ k-mesh is taken. For the calculations with the HSE06 functional, which are considerably more demanding than those with PBE and SCAN, the number of k-points is reduced to $2 \times 2 \times 2$. We checked that the accuracy of the lattice parameters is not affected by this choice. The calculation of the non-analytical component of the dynamical matrix requires the determination of Born effective charges and of the dielectric tensor from DFT. An extra supporting grid is incorporated to evaluate augmentation charges to minimize the impact of noise on the forces.

Interatomic force constants (IFC) are computed using the `hiPhive` package [53], which integrates machine learning regression techniques with forces calculated from random atomic distortions within supercells [54–56]. Distorted $2 \times 2 \times 2$ supercells are generated by a Monte Carlo algorithm that penalizes displacements producing too short interatomic distances [57]. We checked that 10 supercells are sufficient to obtain a root mean square deviation for the forces below 18 meV \AA^{-1} . The mean displacement amplitude for each configuration is 0.25 \AA . To compute the Hellmann-Feynman forces, which are essential for obtaining anharmonic IFCs, DFT calculations are carried out in supercells with a $6 \times 6 \times 6$ k-grid for cubic systems and a $4 \times 4 \times 2$ k-mesh for the hexagonal one; with HSE06, such calculations are performed at Γ only. Multilinear regression is applied to fit forces derived from DFT, using the recursive feature elimination algorithm [57]. We evaluate the convergence of the cutoff distances in the force constant potential (FCP) model by examining variations in force errors and phonon frequencies. Cutoff distances of 9.2, 9.1, 6.4, 4.5, and 4.5 \AA for the second, third, fourth, fifth, and sixth order, respectively, are necessary to achieve the desired convergence for Cs_3Sb with PBE. These cutoff distances are subsequently extrapolated based on coordination shells for calculations with the other xc functionals on the remaining binary systems. A wrapper code for `hiPhive` facilitates automation of distorted supercell creation, force calculation using VASP, and the construction of ML-based FCPs [58]. The evaluation of temperature-dependent anharmonic phonon frequencies is performed by integrating self-consistent phonon (SCPH) calculations combined with the second-order to sixth-order IFCs [59, 60]. In the study of ternary systems, only second-order IFCs are required to accurately compute harmonic phonon dispersion.

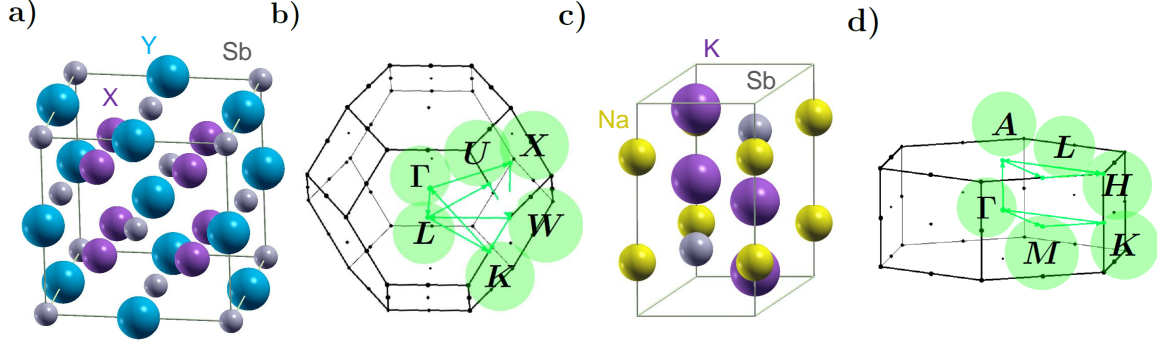


Figure 1: a) Ball-and-stick representation of the conventional unit cell of multi-alkali antimonides with chemical formula X_2YSb ($X = Cs, K, Na$; $Y = Cs, K, Na$) and b) corresponding Brillouin zone with the high-symmetry points and the path connecting them highlighted in green. c) Ball-and-stick representation of the conventional unit cell of NaK_2Sb and d) its Brillouin zone with the high-symmetry points and the path connecting them highlighted in green. Graphics created with `XCrysDen` [61].

3. Results

3.1. Structural properties

In this study on multi-alkali antimonides, we consider three binary systems, Cs_3Sb , K_3Sb , and Na_3Sb , and four ternaries: Cs_2KSb , CsK_2Sb , Na_2Kb , and NaK_2Sb . All materials are modeled in their face-centered cubic (FCC) phase (space group $Fm\bar{3}m$) except for NaK_2Sb which is hexagonal (space group $P6_3/mmc$). The FCC crystals are simulated in their conventional unit cell including 16 atoms (see Figure 1a with the corresponding Brillouin zone in Figure 1b) where Sb atoms are located at the Wyckoff position 4a and the alkali elements at positions 4b and 8c. In the ternary crystals, the sites with coordinates 4b and 8c are occupied by the second alkali species, as illustrated in Figure 1a. In the binary crystals, the alkali species on these sites are inequivalent with respect to the others [24]. The hexagonal crystal structure of NaK_2Sb is described in a conventional unit cell with 8 atoms (see Figure 1c and Brillouin zone in Figure 1d) with Na atoms at 2b positions, K atoms at 4f and Sb atoms at 4f in the Wyckoff notation.

In Table 1, we report the optimized lattice parameters and the unit-cell volumes obtained for the binary crystals using PBE, SCAN, and HSE06 functionals. These results are compared to experimental findings determined by x-ray and electron diffraction techniques [34,63–68]. PBE leads to an overestimation of the lattice constant of Cs_3Sb and K_3Sb by about 0.17 Å and 0.1 Å, respectively. This is a common shortcoming of this approximation that has been extensively reported for various bulk materials [44,69,70]. In the case of Na_3Sb , we obtain a different trend, with the PBE result underestimating the experimental reference by about 0.1 Å. Adopting HSE06 improves the accuracy for Cs_3Sb and in particular for K_3Sb , where the experimental reference is matched (see Table 1). For Na_3Sb , however, HSE06 leads to a further

Table 1: Lattice parameter (a) and unit-cell volume per atom (Ω) of Cs_3Sb , K_3Sb , and Na_3Sb , calculated using DFT with PBE, HSE06, and SCAN functionals and compared to available experimental references.

	PBE	HSE06	SCAN	exp.
Cs₃Sb				
a [Å]	9.348	9.253	9.171	9.14-9.19 ^a
Ω [Å ³ /atom]	50.81	49.51	48.08	47.72-48.51 ^a
K₃Sb				
a [Å]	8.587	8.495	8.465	8.49 ^b
Ω [Å ³ /atom]	39.57	38.32	37.91	38.25 ^b
Na₃Sb				
a [Å]	7.308	7.278	7.447	7.40-7.46 ^c
Ω [Å ³ /atom]	24.39	24.09	25.81	25.33-25.95 ^c
^a [62-65]				
^b [66]				
^c [34, 67]				

underestimation of the lattice parameter compared to PBE. It is worth noting that the FCC phase of this material manifests itself at high pressures in contrast to the hexagonal one that is stable at room conditions [34, 67]. We chose this structure rather than the hexagonal one for a direct comparison with the other binary crystals. Lattice parameters and volumes of Cs_3Sb and Na_3Sb obtained with SCAN are within the experimental range. In the case of K_3Sb , the results obtained with SCAN are a few tenth mÅ below the experimental value but the improvement over PBE and the reduced costs compared to HSE06 make it the best choice.

Table 2: Conventional lattice parameters (a and c for the hexagonal crystal only) and unit-cell volumes per atom (Ω) obtained with the SCAN functional for Cs_2KSb , CsK_2Sb , NaK_2Sb , and Na_2KSb . Available experimental values taken from Refs. [71, 72] are reported in parentheses.

	Cs ₂ KSb	CsK ₂ Sb	NaK ₂ Sb	Na ₂ KSb
a [Å]	9.11	8.62 (8.61 ^a)	5.58 (5.61 ^b)	7.60 (7.72 ^b)
c [Å]			10.92 (10.93 ^b)	
Ω [Å ³ /atom]	50.81	40.03 (39.89 ^a)	36.74 (37.31 ^b)	27.44 (28.76 ^b)

^a [71].

^b [72].

Having identified SCAN as the optimal xc functional to accurately describe the lattice parameters of the binary systems, we employ it to determine the structural properties (lattice constants and volumes) of the considered ternary alkali antimonides (see Table 2). Excellent agreement is found for CsK₂Sb where the calculated values match almost perfectly the experimental references. The results obtained for the in-plane (*a*) and out-of-plane (*c*) lattice parameters of NaK₂Sb are in equally good agreement with measurements. A slight discrepancy of 0.12 Å with respect to the measurement is found for the lattice constant of Na₂KSb (see Table 2): however, it cannot be considered detrimental due to the scarcity of experimental references. For Cs₂KSb, no direct measurements of the lattice constant are available. An interpolated value of 8.88 Å is reported in Ref. [73]: although it is not far from our prediction (see Table 2), we do not consider it a reliable point of comparison. The structural parameters obtained with SCAN for the ternary alkali antimonides considered in this work are in better agreement with the available experimental references than earlier DFT studies adopting semi-local functionals [17, 25, 27, 28, 37, 38, 46, 73].

3.2. Phonon dispersions

To assess the performance of the three considered xc functionals in the calculation of the vibrational properties of multi-alkali antimonides, we evaluate the phonon dispersions of the binary systems. The harmonic approximation predicts a dynamic instability of Cs₃Sb revealed by imaginary frequencies (displayed as negative values) ranging from 0 to 0.7i THz with minima at the high-symmetry points X, K, and U (see Figure 2a). This behavior is independent of the choice of the functional, although the imaginary minima obtained with SCAN are higher in frequency compared to those delivered by PBE and HSE06. By inspecting the harmonic PDOS on the right side of Figure 2a, we identify the predominant contribution of Cs atoms in the low-frequency region, while Sb atoms have a stronger influence at higher frequencies. This behavior is consistent with the masses of the two atomic species.

Phonon frequencies are closely related to the bond strengths: the tighter the interactions, the higher the frequencies. The known over-softening featured by PBE results can be attributed to two main factors: (i) the underestimation of bond strengths as a consequence of overestimated lattice parameters (see Table 1) and (ii) the tendency of this functional to overestimate the electronic polarizability (see Table 1 in the Supporting Information), which amplifies the resonant bonding characteristics [74]. Both SCAN and HSE06 correct the over-softening of PBE (see Figure 2a), due to their more accurate assessment of intermediate- and long-range interactions, as demonstrated in previous studies [75–77].

Using SCPH, we calculate the anharmonic phonon dispersions of Cs₃Sb at increasing temperatures using the three different functionals, see Figures 2b-d. Corrections from quartic, quintic, and sextic IFCs are included and, regardless of the chosen form for v_{xc} , they lift the dynamical instability featured in the harmonic

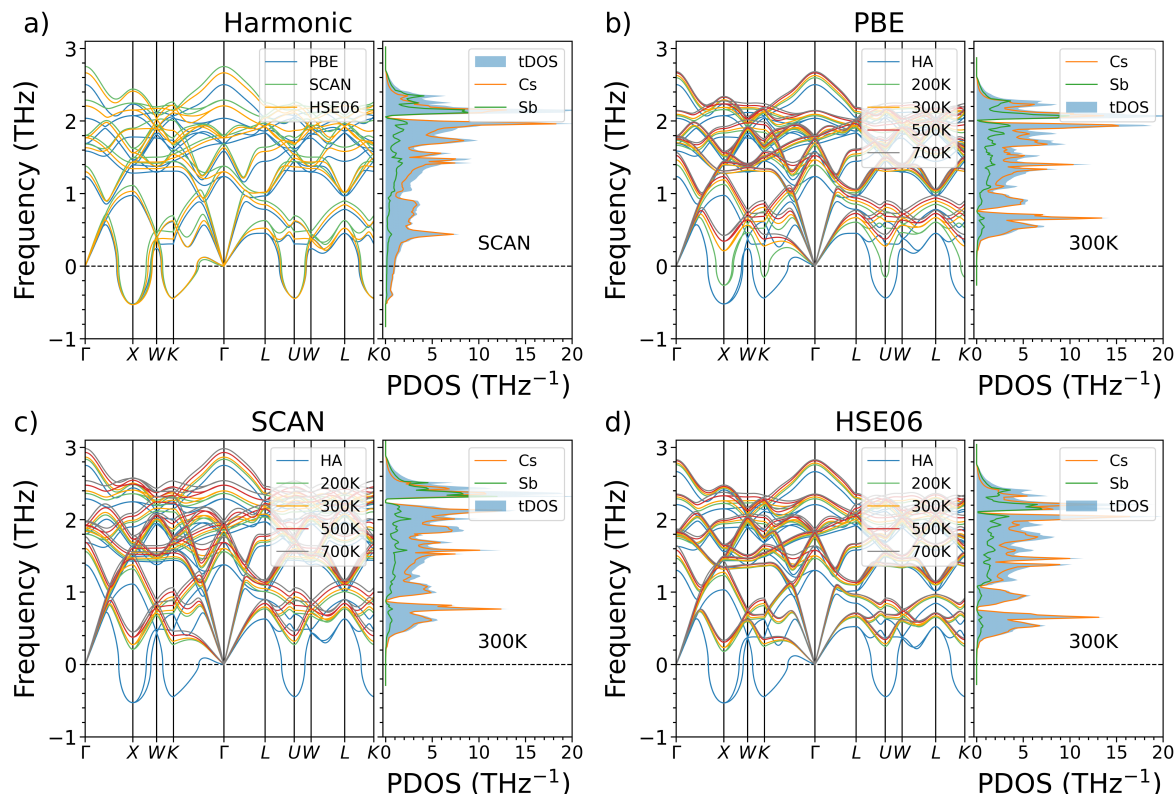


Figure 2: a) Harmonic phonon band structure (left) and atom-projected projected density of states (PDOS) of Cs_3Sb computed with different xc functionals. Temperature-dependent phonon dispersion of Cs_3Sb obtained with b) PBE, c) SCAN, and d) HSE06 in the harmonic (HA) dispersion and with anharmonic contributions at 200 K, 300 K, 500 K, and 700 K. On the right side of panels b)-d), the anharmonic phonon PDOS at 300 K is reported.

approximation [38]. However, the temperature at which imaginary phonon frequencies disappear from the spectra depends on the adopted functional. With PBE, the phonon dispersion computed at 200 K is qualitatively analogous to the one obtained with harmonic contributions only (Figure 2b), and the dynamical instability is lifted at 230 K. With SCAN and HSE06, this threshold temperature is below 200 K and equal to 170 K and 190 K, respectively (see Figures 2c,d). The most significant differences in the phonon dispersions calculated with different functionals appear at the Γ point and are mainly due to longitudinal/transverse (LO/TO) splitting of the optical phonons. These changes reflect alterations in electronic polarization, dielectric tensor, and Born effective charges, as expected from the different functionals [78]. The results obtained with SCAN and HSE06 for Cs_3Sb are overall very similar both in the harmonic approximation as well as when anharmonic corrections are included (Figure 2c-d). Nonetheless, due to its lower computational costs, comparable to those of semi-local DFT, the SCAN functional represents the optimal choice to perform these calculations.

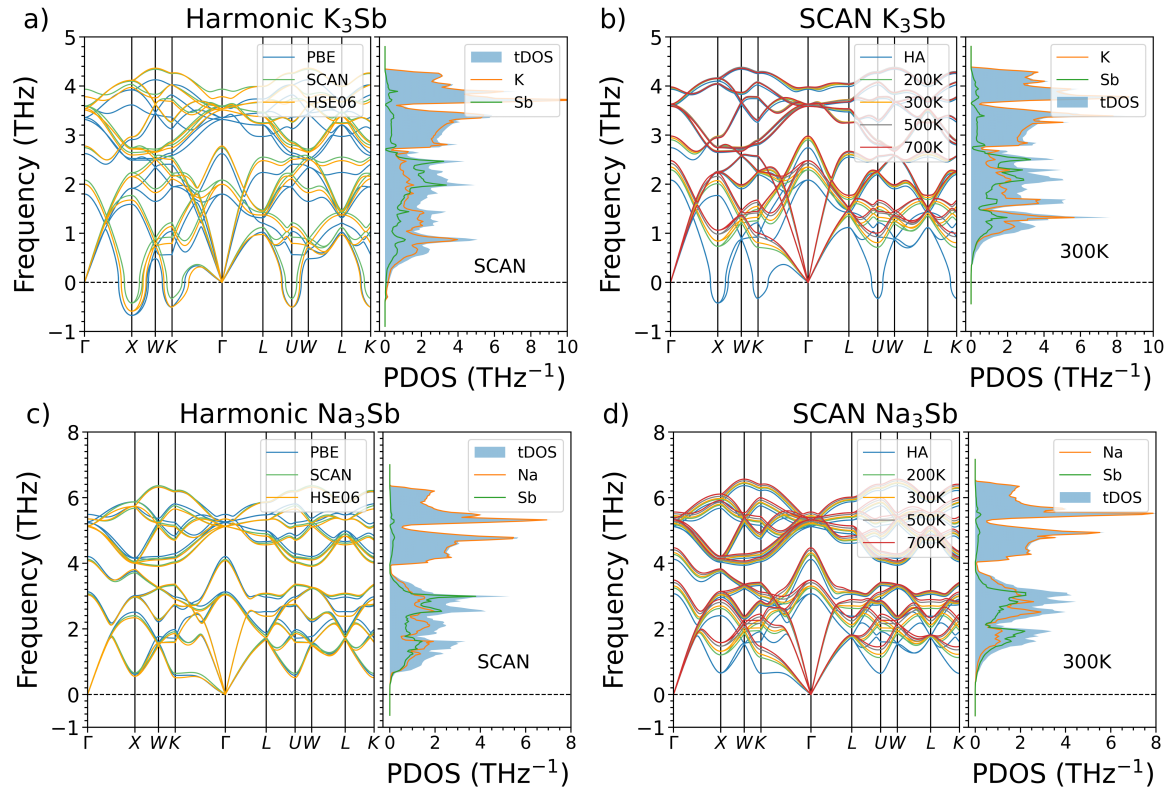


Figure 3: Harmonic phonon dispersion computed with different xc functionals for a) K_3Sb and c) Na_3Sb , and temperature-dependent phonon dispersion (result in the harmonic approximation, HA, shown for comparison) obtained with SCAN for b) K_3Sb and d) Na_3Sb .

The phonon dispersion of K_3Sb in the harmonic approximation (see Figure 3a), closely resembles that of Cs_3Sb (compare Figure 2a), with imaginary frequencies emerging within the same range and exhibiting minima at identical high-symmetry points. The comparison among results obtained with different functionals highlights differences in the LO/TO splitting at the Γ point. For instance, by inspecting the PDOS, it is evident that the lighter atom K contributes more significantly at higher frequencies (see Figure 3a, right panel) compared to Cs (Figure 2a), as expected. The temperature-dependent anharmonic phonon dispersion of K_3Sb obtained with SCAN (see Figure 3b) reveals that the inclusion of higher-order IFCs leads to the disappearance of imaginary frequencies at a lower temperature compared to Cs_3Sb . Temperature-dependent phonon dispersions for K_3Sb obtained with HSE06 and PBE are similar to those obtained with SCAN (see Figure S1 in the Supporting Information).

For Na_3Sb , the situation is different. In the harmonic approximation (Figure 3c), the absence of imaginary frequencies highlights the dynamic stability of this material in contrast to all the other binary alkali antimonides considered in this work and in the literature [79]. This characteristic of Na_3Sb can be attributed to the small atomic radius of Na, which reduces steric hindrance and repulsive interactions, contributing to a more

stable structural arrangement. Furthermore, examining the PDOS in Figure 3c, it is evident that Na contributes more than Sb at higher frequencies, in contrast to heavier alkali atoms that contribute especially in the low-frequency range. Na_3Sb shows a weaker temperature dependence compared to other binary compounds, as shown in Figure 3d. Due to the more pronounced harmonic characteristics of the material, intermediate and long-range interactions are less significant compared to heavier alkali antimonides, leading to minor disparities among results obtained with different xc functional (see Figure S2 in the Supporting Information). We also checked that the qualitative features of the phonon PDOS of the binary alkali antimonides considered in this work are rather insensitive to temperature (see Figure S3).

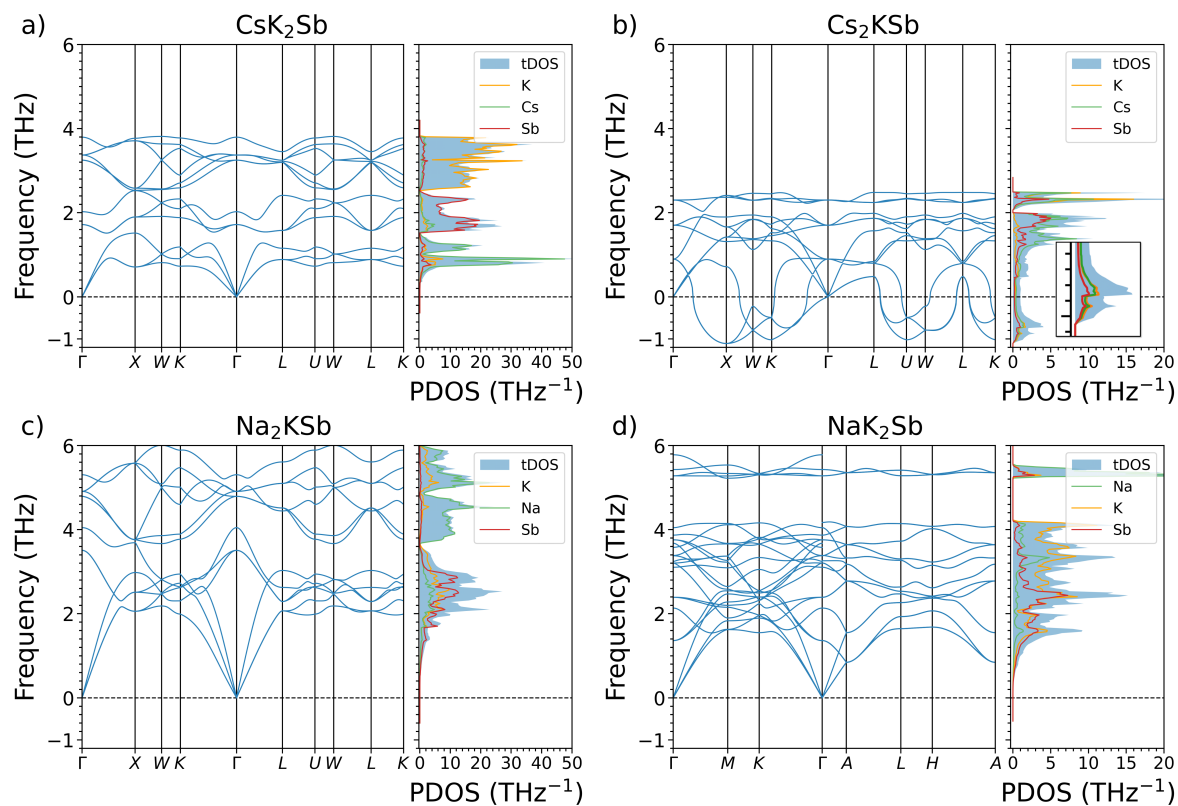


Figure 4: Harmonic phonon dispersions and PDOS of a) CsK_2Sb , b) Cs_2KSb , c) Na_2KSb , and d) NaK_2Sb computed at 0 K with the SCAN functional.

With the insight gained from the binary systems, we now proceed with the analysis of the ternary compounds adopting only the SCAN functional, which offers the optimal trade-off between accuracy and computational efficiency. In Figure 4, we show the phonon band structures and PDOS computed at 0 K in the harmonic approximation. Except for Cs_2KSb , which exhibits imaginary phonon frequencies (Figure 4b), the other three crystals are dynamically stable. In the following, we discuss their vibrational features in detail. The phonon spectrum of CsK_2Sb (Figure 4a) is characterized by three distinct regions. The acoustic modes forming the lowest-energy band (0 - 1.4 THz) are

dominated by Cs contributions, while the low- and high-frequency optical modes (1.4 - 2.2 THz and 2.2 - 3.6 THz) are mainly related to Sb and K atoms, respectively, in line with their atomic masses. A clear separation between acoustic and optical branches occurs along the Γ -X, Γ -K, and Γ -L directions. This characteristic, termed “avoided crossing”, flattens the corresponding phonon bands and reduces the group velocity of the acoustic phonons and, consequently, the lattice thermal conductivity, thereby enhancing the electronic and thermal transport properties of the material [37, 39]. In CsK₂Sb, a distinct separation between optical and acoustic modes is observed, with an evident LO/TO splitting at the Γ point. This feature suggests strong long-range electrostatic interactions within its lattice. The occurrence of imaginary modes within the harmonic approximation for CsK₂Sb is documented in previous DFT studies [39], where the stabilization of this system was achieved by incorporating higher-order force constants using the PBEsol functional. In contrast to these results, our study adopting the SCAN functional does not reveal any imaginary frequencies in the harmonic approximation, highlighting the importance of a suitable xc potential to obtain reliable results.

The phonon dispersion for Cs₂KSb (see Figure 4b), exhibits imaginary frequencies ranging from 0 to 1.1i THz, with notable minima at the high-symmetry points X, K, U, and W. This finding points to a dynamical instability of Cs₂KSb mainly influenced by Cs and K atoms, as evidenced in the PDOS on the right side of Figure 4b. Although Cs₂KSb shares the same crystal structure as CsK₂Sb, the instability of the former material is enhanced by the predominance of Cs atoms over K. Notably, Cs atoms exhibit a larger atomic displacement parameter than K [39]. This larger displacement from the equilibrium position of the Cs atoms leads to a “rattling”, characterized by large amplitude vibrations of weakly bound atoms. This behavior contributes to the softening of the acoustic phonon branches and introduces pronounced anharmonic effects, as has been already reported in other DFT studies [39, 80].

Na₂KSb is structurally identical to its Cs-based counterpart but in contrast to the latter, it is dynamically stable. The phonon dispersion of this material, shown in Figure 4c, features two main regions. Both acoustic and optical modes are found in the low-frequency range (0 - 3.5 THz). The latter are dominated by Sb modes with non-negligible contributions from the alkali species, while all atoms participate almost equally in the acoustic modes. The optical modes at higher frequencies (3.5 - 5.8 THz) are mainly due to Na vibrations with K contributions becoming more relevant above 5 THz; the effect of Sb atoms is negligible in this region. The phonon dispersion of Na₂KSb exhibits a significant LO/TO splitting, which is the most prominent among the ternary compounds investigated in this work. This feature hints at strong long-range electrostatic forces within the lattice structure of Na₂KSb, in agreement with previous DFT studies [36]. This prominence in LO/TO splitting is also indicative of a heightened ionic character in Na₂KSb, which aligns with the high static dielectric constant (see Table S1).

In Figure 4d, the DFT phonon dispersion of hexagonal NaK₂Sb is reported for the first time, according to the best of our knowledge. Due to the larger number of

atoms in this crystal compared to the cubic ones analyzed above, many more modes appear in the band structure. Acoustic and optical modes are seamlessly found in the region 0 - 4.5 THz with mostly K-Sb and Na-Sb contributions below 3 THz and between 3.5 and 4.5 THz, and with a K predominance around 3 THz. A separate manifold of optical phonon bands, mostly related to Na-centered modes, appears around 5 THz. Overall, this hexagonal crystal exhibits flatter phonon bands compared to cubic Na_2Kb . However, the atomic contributions in the various frequency regions are consistent in the two materials, confirming that this characteristic is mainly related to the composition rather than to the stoichiometry and/or the crystalline arrangement.

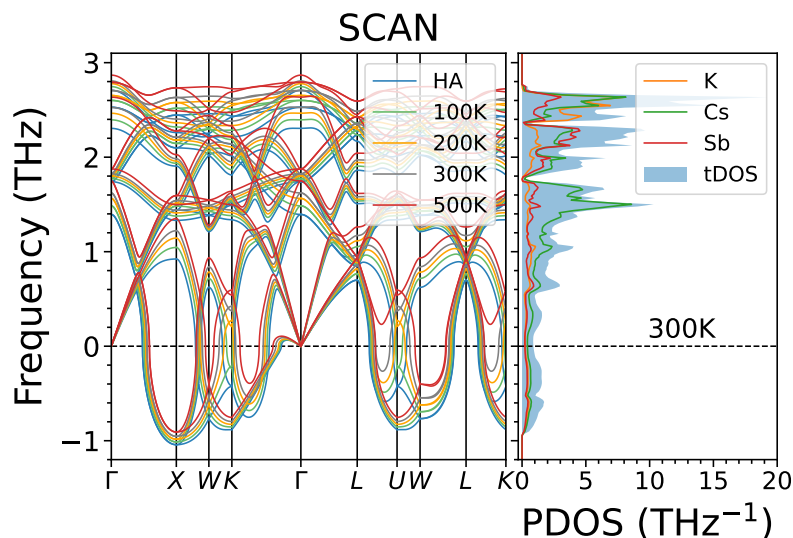


Figure 5: Phonon dispersion of Cs_2KSb obtained with the SCAN functional in the harmonic approximation (HA) and including anharmonic contributions at 100 K, 200 K, 300 K, and 500 K. The atom-resolved PDOS displayed on the right panel corresponds to the anharmonic result at 300 K.

In the last part of this study, we deepen the analysis on Cs_2KSb , which is dynamically unstable at 0 K (see Figure 4b). To this end, we computed the anharmonic phonon dispersion of this material at increasing temperatures including cubic, quartic, quintic, and sextic IFCs. All results shown in Figure 5 feature imaginary modes confirming the instability of Cs_2KSb regardless of temperature. A trend of increasing (negative) frequencies is seen with increasing temperature but even at 500 K, the lowest minima remain well below zero (0.8i THz). The persistence of imaginary modes indicates the inherent dynamic instability of the crystal, which occurs because the structure is located at a local maximum or a saddle point in the potential energy surface (PES). To explore other possible stable configurations, it is crucial to conduct a thorough examination of the PES, for example, by perturbing the crystal structure along a specific phonon eigenvector. This procedure, commonly known as “mode-mapping”, enables sampling the PES based on the amplitude of the harmonic mode [81] and will be the subject of dedicated future work. These findings obtained for Cs_2KSb suggest that, in

contrast to the Na-based counterpart which is predicted to be stable already at 0 K, this material is unstable even at and beyond room temperature and thus not favored during growth. This outcome is in agreement with empirical notions [6].

4. Conclusions

In summary, we investigated the thermodynamic and vibrational properties of binary and ternary alkali antimonide crystals by means of DFT and machine learning methods going beyond the harmonic approximation. We assessed the performance of different exchange-correlation functionals, including PBE, HSE06, and SCAN, in determining the structural parameters and the phonon dispersion of the binary systems. Having found that SCAN offers the optimal trade-off between accuracy and computational efforts, we used it to study the ternary compounds. The phonon band structures and the atom-resolved density of states reveal a clear correlation between Cs content and dynamical stability. Specifically, crystals with a higher Cs concentration are less stable than the others and exhibit imaginary phonon frequencies. While in Cs_3Sb these instabilities are resolved going beyond the harmonic approximation, Cs_2KSb remains unstable even above room temperature, matching the observation that this compound does not form upon evaporation. More in-depth studies exploring the potential energy surface of this compound are required to identify a stable structure. In general, we found that an increase in the atomic mass of the alkali metals leads to a decrease in the energies of the low-lying phonon modes associated with these species. We also provided the first DFT results for the phonon properties of hexagonal NaK_2Sb , which appears to be stable already in the harmonic approximation.

To conclude, our results offer valuable indications about the thermodynamic stability of multi-alkali antimonides. The insight gained from the analysis of their phonon dispersions and density of states can contribute to refining the growth recipes of these materials as well as the prediction of their photoemission yield. From a theoretical perspective, the benchmark of the DFT functional on the thermodynamic and vibrational properties of alkali antimonides complements the findings of an earlier study focused only on their electronic characteristics [46] and promotes SCAN as the optimal choice for the study of these materials even in a high-throughput framework [26, 35].

Acknowledgement

This work was funded by the German Research Foundation, project numbers 490940284 and 182087777 (CRC 951), by the German Federal Ministry of Education and Research (Professorinnenprogramm III), and by the State of Lower Saxony (Professorinnen für Niedersachsen, SMART, and DyNano). J.S.A. acknowledges support from the Evonik Stiftung. The computational resources were provided by the North-German Supercomputing Alliance (HLRN), project nic00076, and by the high-performance

computing cluster CARL at the University of Oldenburg, funded by the German Research Foundation (Project No. INST 184/157-1 FUGG) and by the Ministry of Science and Culture of the State of Lower Saxony.

References

- [1] P. Musumeci, J. Giner Navarro, J.B. Rosenzweig, L. Cultrera, I. Bazarov, J. Maxson, S. Karkare, and H. Padmore. Advances in bright electron sources. *Nucl. Instrum. Methods Phys. Res. A*, 907:209–220, 18.
- [2] Jana Schaber, Rong Xiang, and Nikolai Gaponik. Review of photocathodes for electron beam sources in particle accelerators. *J. Mater. Chem. C*, 11:3162–3179, 2023.
- [3] Sandeep Kumar Mohanty, Mikhail Krasilnikov, Anne Oppelt, Frank Stephan, Daniele Sertore, Laura Monaco, Carlo Pagani, and Wolfgang Hillert. Development and characterization of multi-alkali antimonide photocathodes for high-brightness rf photoinjectors. *Micromachines*, 14(6):1182, 2023.
- [4] Md Abdullah A. Mamun, Abdelmageed A. Elmustafa, Carlos Hernandez-Garcia, Russell Mammei, and Matthew Poelker. Effect of Sb thickness on the performance of bi-alkali-antimonide photocathodes. *J. Vac. Sci. Technol. A*, 34(2):021509, 01 2016.
- [5] M Gaowei, Z Ding, S Schubert, HB Bhandari, J Sinsheimer, J Kuehn, VV Nagarkar, MSJ Marshall, J Walsh, EM Muller, et al. Synthesis and x-ray characterization of sputtered bi-alkali antimonide photocathodes. *APL Mater.*, 5(11), 2017.
- [6] Martin AH Schmeißer, Sonal Mistry, Hans Kirschner, Susanne Schubert, Andreas Jankowiak, Thorsten Kamps, and Julius Kühn. Towards the operation of cs-k-sb photocathodes in superconducting rf photoinjectors. *Phys. Rev. Accel. Beams*, 21(11):113401, 18.
- [7] Luca Cultrera, Siddharth Karkare, Hyeri Lee, Xianghong Liu, Ivan Bazarov, and B Dunham. Cold electron beams from cryocooled, alkali antimonide photocathodes. *Phys. Rev. Accel. Beams*, 18(11):113401, 2015.
- [8] Z Ding, M Gaowei, J Sinsheimer, J Xie, S Schubert, H Padmore, E Muller, and John Smedley. In-situ synchrotron x-ray characterization of K2CsSb photocathode grown by ternary co-evaporation. *J. Appl. Phys.*, 121(5):055305, 17.
- [9] Jun Feng, Siddharth Karkare, James Nasiatka, Susanne Schubert, John Smedley, and Howard Padmore. Near atomically smooth alkali antimonide photocathode thin films. *J. Appl. Phys.*, 121(4):044904, 17.
- [10] S. Schubert, M. Ruiz-Osés, I. Ben-Zvi, T. Kamps, X. Liang, E. Muller, K. Müller, H. Padmore, T. Rao, X. Tong, T. Vecchione, and J. Smedley. Bi-alkali antimonide photocathodes for high brightness accelerators. *APL Mater.*, 1(3):032119, 09 2013.
- [11] M. Ruiz-Osés, S. Schubert, K. Attenkofer, I. Ben-Zvi, X. Liang, E. Muller, H. Padmore, T. Rao, T. Vecchione, J. Wong, J. Xie, and J. Smedley. Direct observation of bi-alkali antimonide photocathodes growth via in operando x-ray diffraction studies. *APL Mater.*, 2(12):121101, 12 2014.
- [12] Luca Cultrera, Ivan Bazarov, Adam Bartnik, Bruce Dunham, Siddharth Karkare, Richard Merluzzi, and Matthew Nichols. Thermal emittance and response time of a cesium antimonide photocathode. *Appl. Phys. Lett.*, 99(15), 2011.
- [13] Ivan Bazarov, Luca Cultrera, Adam Bartnik, Bruce Dunham, Siddharth Karkare, Yulin Li, Xianghong Liu, Jared Maxson, and William Roussel. Thermal emittance measurements of a cesium potassium antimonide photocathode. *Appl. Phys. Lett.*, 98(22):224101, 11.
- [14] T Vecchione, I Ben-Zvi, DH Dowell, J Feng, T Rao, J Smedley, W Wan, and HA Padmore. A low emittance and high efficiency visible light photocathode for high brightness accelerator-based x-ray light sources. *Appl. Phys. Lett.*, 99(3):034103, 11.
- [15] Jun Dai, Yikun Ding, Cunjun Ruan, Xiangyan Xu, and Hulin Liu. High photocurrent density

- and continuous electron emission characterization of a multi-alkali antimonide photocathode. *Electronics*, 9(12):1991, 2020.
- [16] E Wang, VN Litvinenko, I Pinayev, M Gaowei, J Skaritka, S Belomestnykh, I Ben-Zvi, JC Brutus, Y Jing, J Biswas, et al. Long lifetime of bi-alkali photocathodes operating in high gradient superconducting radio frequency gun. *Sci. Rep.*, 11(1):4477, 2021.
- [17] Caterina Cocchi, Sonal Mistry, Martin Schmeißer, Raymond Amador, Julius Kühn, and Thorsten Kamps. Electronic structure and core electron fingerprints of caesium-based multi-alkali antimonides for ultra-bright electron sources. *Sci. Rep.*, 9(1):18276, 19.
- [18] H Panuganti, E Chevallay, V Fedosseev, and M Himmerlich. Synthesis, surface chemical analysis, lifetime studies and degradation mechanisms of cs-k-sb photocathodes. *Nucl. Instrum. Methods Phys. Res. A*, 986:164724, 2021.
- [19] VS Rusetsky, VA Golyashov, SV Ereemeev, DA Kustov, IP Rusinov, TS Shamirzaev, AV Mironov, A Yu Demin, and OE Tereshchenko. New spin-polarized electron source based on alkali antimonide photocathode. *Phys. Rev. Lett.*, 129(16):166802, 2022.
- [20] L. Kalarasse, B. Bennecer, and F. Kalarasse. Optical properties of the alkali antimonide semiconductors Cs₃Sb, Cs₂KSb, CsK₂Sb and K₃Sb. *J. Phys. Chem. Solids*, 71(3):314–322, 10.
- [21] San-Dong Guo. Electronic structures and elastic properties of X₃Sb (X = Li, K, Cs) from the first-principles calculations. *Mater. Res. Express*, 1(1):015906, 14.
- [22] G Murtaza, Mazhar Ullah, Naeem Ullah, Malika Rani, M Muzammil, R Khenata, Shahid M Ramay, and Umair Khan. Structural, elastic, electronic and optical properties of bi-alkali antimonides. *Bull. Mater. Sci.*, 39:1581–1591, 2016.
- [23] Caterina Cocchi, Sonal Mistry, Martin Schmeißer, Julius Kühn, and Thorsten Kamps. First-principles many-body study of the electronic and optical properties of CsK₂Sb, a semiconducting material for ultra-bright electron sources. *J. Phys.: Condens. Matter.*, 31(1):014002, 18.
- [24] Caterina Cocchi. X-ray absorption fingerprints from cs atoms in cs₃sb. *Phys. Status Solidi (RRL)*, 14(7):2000194, 2020.
- [25] Raymond Amador, Holger-Dietrich Saßnick, and Caterina Cocchi. Electronic structure and optical properties of Na₂KSb and NaK₂Sb from first-principles many-body theory. *J. Phys.: Condens. Matter.*, 33(36):365502, 21.
- [26] Caterina Cocchi and Holger-Dietrich Saßnick. Ab Initio Quantum-Mechanical Predictions of Semiconducting Photocathode Materials. *Micromachines*, 12(9):1002, 21.
- [27] Richard Schier, Holger-Dietrich Saßnick, and Caterina Cocchi. Stability and electronic properties of csk₂sb surface facets. *Phys. Rev. Mater.*, 6(12):125001, 22.
- [28] Ruiqi Wu and Alex M Ganose. Relativistic electronic structure and photovoltaic performance of k₂cssb. *J. Mater. Chem. A*, 11(40):21636–21644, 2023.
- [29] DA Dimitrov, GI Bell, J Smedley, I Ben-Zvi, J Feng, S Karkare, and HA Padmore. Modeling quantum yield, emittance, and surface roughness effects from metallic photocathodes. *J. Appl. Phys.*, 122(16), 2017.
- [30] Kevin L Jensen, Daniel Finkenstadt, Andrew Shabaev, Samuel G Lambrakos, Nathan A Moody, John J Petillo, Hisato Yamaguchi, and Fangze Liu. A photoemission moments model using density functional and transfer matrix methods applied to coating layers on surfaces: Theory. *J. Appl. Phys.*, 123(4), 2018.
- [31] Evan R. Antoniuk, Yumeng Yue, Yao Zhou, Peter Schindler, W. Andreas Schroeder, Bruce Dunham, Piero Pianetta, Theodore Vecchione, and Evan J. Reed. Generalizable density functional theory based photoemission model for the accelerated development of photocathodes and other photoemissive devices. *Phys. Rev. B*, 101(23):235447, 20.
- [32] J Kevin Nangoi, Siddharth Karkare, Ravishankar Sundararaman, Howard A Padmore, and Tomás A Arias. Importance of bulk excitations and coherent electron-photon-phonon scattering in photoemission from pbte (111): Ab initio theory with experimental comparisons. *Phys. Rev. B*, 104(11):115132, 2021.

- [33] Pallavi Saha, Oksana Chubenko, J Kevin Nangoi, Tomas Arias, Eric Montgomery, Shashi Poddar, Howard A Padmore, and Siddharth Karkare. Theory of photoemission from cathodes with disordered surfaces. *J. Appl. Phys.*, 133(5), 2023.
- [34] Riccarda Caputo. An insight into sodiation of antimony from first-principles crystal structure prediction. *J. Electron. Mater.*, 45:999–1010, 2016.
- [35] Holger-Dietrich Saßnick and Caterina Cocchi. Exploring cesium–tellurium phase space via high-throughput calculations beyond semi-local density-functional theory. *J. Chem. Phys.*, 156(10), 2022.
- [36] Tongcai Yue, Pengfei Sui, Yinchang Zhao, Jun Ni, Sheng Meng, and Zhenhong Dai. Theoretical prediction of mechanics, transport, and thermoelectric properties of full heusler compounds na_2ksb and x_2cssb ($\text{x} = \text{k}, \text{rb}$). *Phys. Rev. B*, 105(18):184304, 22.
- [37] Gautam Sharma, Muhammad Sajjad, and Nirpendra Singh. Impressive electronic and thermal transports in csk_2sb : A thermoelectric perspective. *ACS Appl. Electron. Mater.*, 6(21):11179–11188, 23.
- [38] Qi Zhong, Zhenhong Dai, Weiqiang Wang, Yinchang Zhao, and Sheng Meng. Quartic anharmonicity and ultra-low lattice thermal conductivity of alkali antimonide compounds m_3sb ($\text{m} = \text{k}, \text{rb}$ and cs). *Int. J. Energy Res.*, 45(5):6958–6965, 21.
- [39] Kunpeng Yuan, Xiaoliang Zhang, Zheng Chang, Dawei Tang, and Ming Hu. Antibonding induced anharmonicity leading to ultralow lattice thermal conductivity and extraordinary thermoelectric performance in csk_2x ($\text{x} = \text{sb}, \text{bi}$). *J. Mater. Chem. C*, 10(42):15822–15832, 22.
- [40] W. Kohn and L. J. Sham. Self-consistent equations including exchange and correlation effects. *Phys. Rev.*, 140(4A):A1133–A1138, November 65.
- [41] P. Hohenberg and W. Kohn. Inhomogeneous electron gas. *Phys. Rev.*, 136(3B):B864–B871, 64.
- [42] John P. Perdew, Kieron Burke, and Matthias Ernzerhof. Generalized gradient approximation made simple. *Phys. Rev. Lett.*, 77(18):3865–3868, 96.
- [43] Jianwei Sun, Adrienn Ruzsinszky, and John P. Perdew. Strongly constrained and appropriately normed semilocal density functional. *Phys. Rev. Lett.*, 115(3):036402, 15.
- [44] Guo-Xu Zhang, Anthony M. Reilly, Alexandre Tkatchenko, and Matthias Scheffler. Performance of various density-functional approximations for cohesive properties of 64 bulk solids. *New. J. Phys.*, 20(6):063020, 18.
- [45] Mohan Chen, Hsin-Yu Ko, Richard C. Remsing, Marcos F. Calegari Andrade, Biswajit Santra, Zhaoru Sun, Annabella Selloni, Roberto Car, Michael L. Klein, John P. Perdew, and Xifan Wu. Ab initio theory and modeling of water. *Proc. Natl. Acad. Sci. USA*, 114(41):10846–10851, 17.
- [46] Holger-Dietrich Saßnick and Caterina Cocchi. Electronic structure of cesium-based photocathode materials from density functional theory: Performance of pbe, scan, and hse06 functionals. *Electron. Struct.*, 3(2):027001, June 21.
- [47] Jochen Heyd, Gustavo E. Scuseria, and Matthias Ernzerhof. Hybrid functionals based on a screened Coulomb potential. *J. Chem. Phys.*, 118(18):8207–8215, 03.
- [48] Jochen Heyd, Gustavo E. Scuseria, and Matthias Ernzerhof. Erratum: “Hybrid functionals based on a screened Coulomb potential” [*J. Chem. Phys.* 118, 8207 (2003)]. *J. Chem. Phys.*, 124(21):219906, 06 2006.
- [49] G. Kresse and J. Hafner. *Ab Initio* molecular dynamics for liquid metals. *Phys. Rev. B*, 47(1):558–561, 93.
- [50] G. Kresse and J. Furthmüller. Efficiency of ab-initio total energy calculations for metals and semiconductors using a plane-wave basis set. *Comp. Mater. Sci.*, 6(1):15–50, 96.
- [51] G. Kresse and J. Furthmüller. Efficient iterative schemes for ab initio total-energy calculations using a plane-wave basis set. *Phys. Rev. B*, 54(16):11169–11186, 96.
- [52] G. Kresse and D. Joubert. From ultrasoft pseudopotentials to the projector augmented-wave method. *Phys. Rev. B*, 59(3):1758–1775, 99.
- [53] Fredrik Eriksson, Erik Fransson, and Paul Erhart. The Hiphive Package for the Extraction of High-Order Force Constants by Machine Learning. *Adv. Theory Simul.*, 2(5), 19.

- [54] Jose J. Plata, Victor Posligua, Antonio M. Márquez, Javier Fernandez Sanz, and Ricardo Grau-Crespo. Charting the lattice thermal conductivities of i-iii-vi2 chalcopyrite semiconductors. *Chem. Mater.*, 34(6):2833–2841, March 22.
- [55] Jose J. Plata, Ernesto J. Blancas, Antonio M. Márquez, Victor Posligua, Javier Fdez Sanz, and Ricardo Grau-Crespo. Harnessing the unusually strong improvement of thermoelectric performance of aginte2 with nanostructuring. *J. Mater. Chem. A*, 11(31):16734–16742, 23.
- [56] Joakim Brorsson, Arsalan Hashemi, Zheyong Fan, Erik Fransson, Fredrik Eriksson, Tapio AlaNissila, Arkady V. Krasheninnikov, Hannu-Pekka Komsa, and Paul Erhart. Efficient Calculation of the Lattice Thermal Conductivity by Atomistic Simulations with Ab Initio Accuracy. *Adv. Theory Simul.*, 5(2):2100217, 22.
- [57] Erik Fransson, Fredrik Eriksson, and Paul Erhart. Efficient construction of linear models in materials modeling and applications to force constant expansions. 6(1):135, 20.
- [58] Jose J. Plata, Victor Posligua, Antonio M. Márquez, Javier Fernandez Sanz, and Ricardo Grau-Crespo. Charting the lattice thermal conductivities of i-iii-vi2 chalcopyrite semiconductors. *Chem. Mater.*, 34(6):2833–2841, 2022.
- [59] Keivan Esfarjani and Harold T. Stokes. Method to extract anharmonic force constants from first principles calculations. *Phys. Rev. B*, 77(14):144112, 08.
- [60] Ion Errea, Matteo Calandra, and Francesco Mauri. Anharmonic free energies and phonon dispersions from the stochastic self-consistent harmonic approximation: Application to platinum and palladium hydrides. *Phys. Rev. B*, 89(6):064302, 14.
- [61] Anton Kokalj. XCrySDen - a new program for displaying crystalline structures and electron densities. *J. Mol. Graphics Modell.*, 17(3):176–179, 99.
- [62] Geert Gnutzmann, Friedrich Wilhelm Dorn, and Wilhelm Klemm. Das verhalten der alkalimetalle zu halbmatalen. VII. Über einige A3B- und AB2-Verbindungen der schweren alkalimetalle mit elementen der V. Gruppe. *Z. Anorg. Allg. Chem.*, 309(3 – 4):210–225, 61.
- [63] J. Sangster and A. D. Pelton. The cs-sb (cesium-antimony) system. *J. Phase Equilibria Diffus.*, 18(4):382–386, 97.
- [64] J C Robbie and A H Beck. Scanning electron diffraction studies on caesium antimonide photocathodes during formation. *J. Phys. D*, 6(11):1381–1392, 73.
- [65] Jean Marc Barois, Claude Fouassier, Marc Onillon, and Bernard Tanguy. Experimental study of the non stoichiometry of cesium antimonide \approx Cs₃Sb. *Mater. Chem. Phys.*, 24(1):189–197, 89.
- [66] A. H. Sommer and W. H. McCarroll. A new modification of the semiconducting compound k3sb. *J. Appl. Phys.*, 37(1):174–179, January 66.
- [67] M E Leonova, I K Bdikin, S A Kulinich, O K Gulish, L G Sevast'yanova, and K P Burdina. High-pressure phase transition of hexagonal alkali pnictides. *Inorg. Mater.*, 39(3), 03.
- [68] Kenneth Henderson Jack, M. M. Wachtel, and William Lawrence Bragg. The characterization and crystal structure of caesium antimonide, a photo-electric surface material. *Proc. R. Soc. London A*, 239(1216):46–60, 57.
- [69] Laurids Schimka, Judith Harl, and Georg Kresse. Improved hybrid functional for solids: The hsesol functional. *J. Chem. Phys.*, 134(2):024116, 11.
- [70] Fabien Tran, Julia Stelzl, and Peter Blaha. Rungs 1 to 4 of dft jacob's ladder: Extensive test on the lattice constant, bulk modulus, and cohesive energy of solids. *J. Chem. Phys.*, 144(20):204120, 16.
- [71] W. H. McCarroll. Chemical and structural characteristics of the potassium-cesium-antimony photocathode. *J. Phys. Chem. Solids*, 26(1):191–195, 65.
- [72] W.H. McCarroll. Phases in the photoelectric sodium-potassium-antimony system. *J. Phys. Chem. Solids*, 16(1-2):30–36, 60.
- [73] A.R.H.F. Ettema and R.A. De Groot. Electronic structure of Cs₂KSb and K₂CsSb. *Phys. Rev. B*, 66(11):115102, 02.
- [74] Sangyeop Lee, Keivan Esfarjani, Tengfei Luo, Jiawei Zhou, Zhiting Tian, and Gang Chen. Resonant bonding leads to low lattice thermal conductivity. *Nature Commun.*, 5(1):3525, 14.

- [75] Yubo Zhang, Jianwei Sun, John P. Perdew, and Xifan Wu. Comparative first-principles studies of prototypical ferroelectric materials by lda, gga, and scan meta-gga. *Phys. Rev. B*, 96(3):035143, 17.
- [76] Jianwei Sun, Richard C. Remsing, Yubo Zhang, Zhaoru Sun, Adrienn Ruzsinszky, Haowei Peng, Zenghui Yang, Arpita Paul, Umesh Waghmare, Xifan Wu, Michael L. Klein, and John P. Perdew. Accurate first-principles structures and energies of diversely bonded systems from an efficient density functional. *Nature Chem.*, 8(9):831–836, 16.
- [77] Xiaofei Shao, Peitao Liu, Cesare Franchini, Yi Xia, and Jiangang He. Assessing the performance of exchange-correlation functionals on lattice constants of binary solids at room temperature within the quasiharmonic approximation. *Phys. Rev. B*, 108(2):024306, July 23.
- [78] Jonathan M. Skelton, Davide Tiana, Stephen C. Parker, Atsushi Togo, Isao Tanaka, and Aron Walsh. Influence of the exchange-correlation functional on the quasi-harmonic lattice dynamics of ii-vi semiconductors. *J. Chem. Phys.*, 143(6), 15.
- [79] Yinchang Zhao, Chao Lian, Shuming Zeng, Zhenhong Dai, Sheng Meng, and Jun Ni. Quartic anharmonicity and anomalous thermal conductivity in cubic antiperovskites a₃bo (a = k, rb; b = br, au). *Phys. Rev. B*, 101(18):184303, 20.
- [80] Annalise E. Maughan, Arnold A. Paecklar, and James R. Neilson. Bond valences and anharmonicity in vacancy-ordered double perovskite halides. *J. Mater. Chem. C*, 6(44):12095–12104, 18.
- [81] Jonathan M. Skelton, Lee A. Burton, Stephen C. Parker, Aron Walsh, Chang-Eun Kim, Aloysius Soon, John Buckeridge, Alexey A. Sokol, C. Richard A. Catlow, Atsushi Togo, and Isao Tanaka. Anharmonicity in the high-temperature cmcn phase of s_nse: Soft modes and three-phonon interactions. *Phys. Rev. Lett.*, 117(7):075502, 16.